Computers & Graphics (2017)

Contents lists available at ScienceDirect

Computers & Graphics

journal homepage: www.elsevier.com/locate/results-in-physics

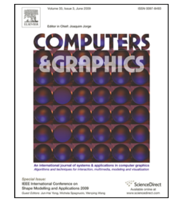

Enhanced Vector Field Visualization via Lagrangian Accumulation Supplemental Material: Discussion and Additional Results

Lei Zhang[1], Duong Nguyen[1], David Thompson[2], Robert Laramee[3], Guoning Chen[1]*

[1]University of Houston, [2]Mississippi State University, [3]Swansea University

ARTICLE INFO

Article history:

ABSTRACT

This document provides additional description to certain content of the paper and additional results of the $\mathscr{A}$ field-based flow visualization.

1. Detailed Derivation of Relation between FTLE and Pathline Orientation Vector

Recall that in Section 5.2 of the paper, the Lagrangian accumulation is applied to collect vector-valued properties. Specifically, we use it to accumulate the flow vectors scaled by the integration step size along the pathlines. The resulting $\mathscr{A}$ field is a vector field. If we consider a forward accumulation with a time window $[t_0, t_0+T]$, the resulted vector at each sampling point is an orientation vector that points from the starting point to the end point of the integral curve [1] based on vector calculus. We denote this vector as $V_{SE}(\mathbf{x}) = \varphi_{t_0}^{t_0+T}(\mathbf{x}) - \varphi_{t_0}^{t_0}(\mathbf{x})$ based on the notion of flow map [2]. After getting this vector-valued $\mathscr{A}$ field, we compute its discrete gradient using finite difference. For simplicity, we consider a 2D regular grid. The discrete gradient of the vector-valued $\mathscr{A}$ field at a sampling point $\mathbf{x} = (x_i, y_j)$ is given as follows

$$
\begin{aligned}
F &= \frac{dV_{SE}(\mathbf{x})}{d\mathbf{x}} = \begin{bmatrix} \frac{Vx_{SE}(\mathbf{x}_{i+1,j}) - Vx_{SE}(\mathbf{x}_{i-1,j})}{x_{i+1,j}(t_0) - x_{i-1,j}(t_0)} & \frac{Vx_{SE}(\mathbf{x}_{i,j+1}) - Vx_{SE}(\mathbf{x}_{i,j-1})}{y_{i,j+1}(t_0) - y_{i,j-1}(t_0)} \\ \frac{Vy_{SE}(\mathbf{x}_{i+1,j}) - Vy_{SE}(\mathbf{x}_{i-1,j})}{x_{i+1,j}(t_0) - x_{i-1,j}(t_0)} & \frac{Vy_{SE}(\mathbf{x}_{i,j+1}) - Vy_{SE}(\mathbf{x}_{i,j-1})}{y_{i,j+1}(t_0) - y_{i,j-1}(t_0)} \end{bmatrix} \\
&= \begin{bmatrix} A & B \\ C & D \end{bmatrix}
\end{aligned} \tag{1}
$$

with

$$
\begin{aligned}
A &= \frac{(x_{i+1,j}(t_0+T) - x_{i-1,j}(t_0+T)) - (x_{i+1,j}(t_0) - x_{i-1,j}(t_0))}{x_{i+1,j}(t_0) - x_{i-1,j}(t_0)} \\
B &= \frac{(x_{i,j+1}(t_0+T) - x_{i,j-1}(t_0+T)) - (x_{i,j+1}(t_0) - x_{i,j-1}(t_0))}{y_{i,j+1}(t_0) - y_{i,j-1}(t_0)} \\
C &= \frac{(y_{i+1,j}(t_0+T) - y_{i-1,j}(t_0+T)) - (y_{i+1,j}(t_0) - y_{i-1,j}(t_0))}{x_{i+1,j}(t_0) - x_{i-1,j}(t_0)} \\
D &= \frac{(y_{i,j+1}(t_0+T) - y_{i,j-1}(t_0+T)) - (y_{i,j+1}(t_0) - y_{i,j_1}(t_0))}{y_{i,j+1}(t_0) - y_{i,j-1}(t_0)}
\end{aligned} \tag{2}
$$

Then,

$$
\begin{aligned}
F &= \frac{d\varphi_{t_0}^{t_0+t}(\mathbf{x})}{d\mathbf{x}} - \begin{bmatrix} \frac{(x_{i+1,j}(t_0) - x_{i-1,j}(t_0))}{x_{i+1,j}(t_0) - x_{i-1,j}(t_0)} & \frac{(x_{i,j+1}(t_0) - x_{i,j-1}(t_0))}{y_{i,j+1}(t_0) - y_{i,j-1}(t_0)} \\ \frac{(y_{i+1,j}(t_0) - y_{i-1,j}(t_0))}{x_{i+1,j}(t_0) - x_{i-1,j}(t_0)} & \frac{(y_{i,j+1}(t_0) - y_{i,j_1}(t_0))}{y_{i,j+1}(t_0) - y_{i,j-1}(t_0)} \end{bmatrix} \\
&= \frac{d\varphi_{t_0}^{t_0+t}(\mathbf{x})}{d\mathbf{x}} - I_2
\end{aligned} \tag{3}
$$

This is because

$$
\frac{d\varphi_{t_0}^{t_0+t}(\mathbf{x})}{d\mathbf{x}} = \begin{bmatrix} \frac{(x_{i+1,j}(t_0+T) - x_{i-1,j}(t_0+T))}{x_{i+1,j}(t_0) - x_{i-1,j}(t_0)} & \frac{(x_{i,j+1}(t_0+T) - x_{i,j-1}(t_0+T))}{y_{i,j+1}(t_0) - y_{i,j-1}(t_0)} \\ \frac{(y_{i+1,j}(t_0+T) - y_{i-1,j}(t_0+T))}{x_{i+1,j}(t_0) - x_{i-1,j}(t_0)} & \frac{(y_{i,j+1}(t_0+T) - y_{i,j-1}(t_0+T))}{y_{i,j+1}(t_0) - y_{i,j-1}(t_0)} \end{bmatrix}
$$

and both $x_{i,j+1}(t_0) - x_{i,j-1}(t_0) = 0$ and $y_{i+1,j}(t_0) - y_{i-1,j}(t_0) = 0$ in a regular grid.

2. Additional Results

Figure 1 provides some additional results on the effects of computing $\mathscr{A}$ fields with different accumulation window sizes.

*Corresponding author
e-mail: gchen16@uh.edu (Guoning Chen[1])

Their corresponding $|\nabla\mathscr{A}|$ fields are also shown to illustrate the patterns of the discontinuity in the respective $\mathscr{A}$ fields.

Figure 2 provides additional result to demonstrate the effect of the anisotropic smoothing during the $\mathscr{A}$ field computation (see Section 5 of the paper). This smoothing is performed in a similar fashion to the enhanced-LIC [3]. That is, for any give sampling point, we compute a short integral curve. If it is a steady flow, we compute a short stream let in both forward and backward flow direction. If it is an unsteady flow, we only consider the forward direction. After getting this short integral curve, we then interpolate the $\mathscr{A}$ values at the individual integration points, and average the accumulated value. This average value is then used to replace the original $\mathscr{A}$ value at the above sampling point. In the example of Figure 2, an $\mathscr{A}$ field is computed on a triangular mesh of the cross section of a diesel engine simulation. The discontinuity in the resulting field has zig-zagged configuration. After performing the anisotropic smoothing, the resulting field has much smoother patterns (right). The $\mathscr{A}$ field computed using a dense uniform sampling strategy is shown in the right image of the top row of (b) in Figure 1.

Figure 3 compares the $\mathscr{A}$ fields obtained by accumulating curl, λ_2, Q and winding angle, respectively, for a synthetic 2D flow. The corresponding detected edges and their $|\nabla\mathscr{A}|$ fields are shown in the second and third rows, respectively. From the results, we can see that λ_2 and Q based $\mathscr{A}$ fields typically draw our attention to the regions near the center of vortices, while the curl and winding angle based $\mathscr{A}$ fields reveal both the vortices and the prominent separation structure near them. In addition, the λ_2 and Q based $\mathscr{A}$ fields possess a large amount of noise, which is captured by the $|\nabla\mathscr{A}|$. This may be explained by the numerical instability in the computation of the λ_2 and Q values.

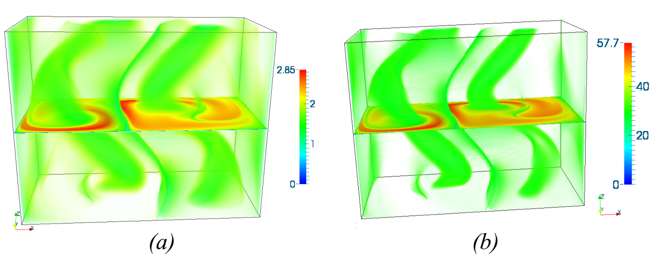

Fig. 4: Comparison of the $\mathscr{A}$ fields of the double gyre flow computed based on the arc-length (a) and the velocity magnitude (b), respectively.

Figure 4 shows a comparison of the $\mathscr{A}$ fields of the double gyre flow computed based on the arc-length (a) and the velocity magnitude (b), respectively. From the result, we see that they have similar behavior. This is not surprising, because the arc-length of each segment of an integral curve is determined by the length of the vector value at the starting point of this segment scaled by the integration step size, i.e., scaled velocity magnitude. Therefore, they are different by a scale factor.

2.1. *Flow Pass a Cylinder*

Figure 5 shows the projected $\mathscr{A}$ and $|\nabla\mathscr{A}|$ fields computed by accumulating the change of the flow direction at time $t=0$ with $T=3$ (a. forward) and $T=-3$ (b. backward), respectively, for the flow behind a cylinder [4]. We compare our results with the forward and backward FTLE fields, and observe that the ridges of the $|\nabla\mathscr{A}|$ fields match closely with the ridges of the FTLE fields, while the $\mathscr{A}$ field encodes additional rotational information that clearly highlights the regions of particles whose trajectories exhibit strong positive (red) or negative (blue) rotations in the spatio-temporal domain.

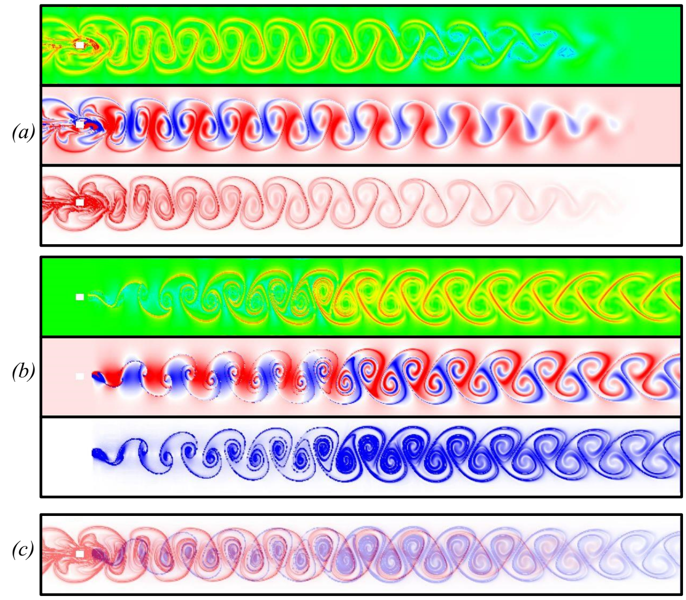

Fig. 5: The analysis results of the flow past a cylinder simulation. (a) shows the forward tracing results ($T=3$) with FTLE in the top row followed by the $\mathscr{A}$ and $|\nabla\mathscr{A}|$ fields. (b) shows the backward tracing results ($T=-3$), and (c) the combination of the forward (red) and backward (blue) ridges of $|\nabla\mathscr{A}|$ fields.

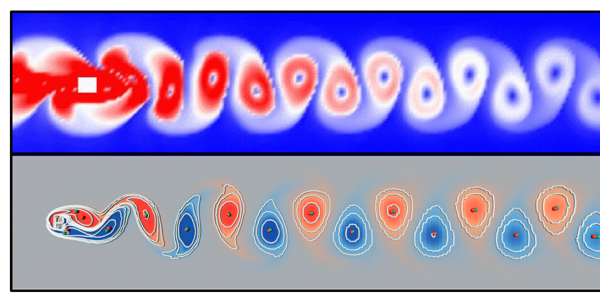

Fig. 6: This figure shows the comparison of the $\mathscr{A}$ field computed using absolute curvature (top) with the vorticity iso-lines from[5] (bottom).

In addition to accumulating signed winding angle along the integral curves, we accumulate the absolute angle difference. This enables us to address the possible cancellation of the accumulation of signed rotation. However, the information about the orientation of the rotation is lost. Figure 6 shows the result of the pathline based $\mathscr{A}$ field (top) computed using time window $T=3$ for the flow behind a cylinder. As expected, instead of showing the regions with different rotation orientations, it simply highlights the regions with strong rotation. We compare our result with the vorticity iso-line extraction [5] (bottom), and see the new $\mathscr{A}$ field highlights the regions of the vortices similar to the vorticity iso-lines. However, the difference is we use *pathlines* instead of streamlines to compute the $\mathscr{A}$ field.

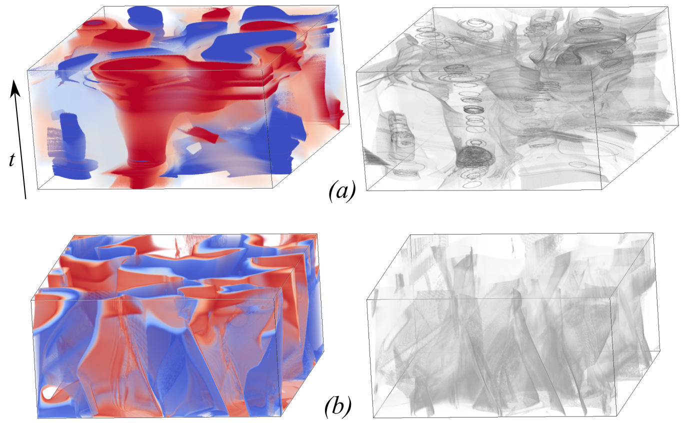

Fig. 7: The volume renderings of two $\mathscr{A}$ (left column) fields and their corresponding $|\nabla\mathscr{A}|$ (right column) fields for the HCCI simulation. Both $\mathscr{A}$ fields are computed by accumulating the signed angle change of the flow direction. (a) shows the volume renderings of an $\mathscr{A}$ and $|\nabla\mathscr{A}|$ fields by stacking the individual 2D fields computed at their respective time steps. This streamline based result clearly highlights the translation and interaction of individual vortices over time. (b) shows the volume renderings of the $\mathscr{A}$ and $|\nabla\mathscr{A}|$ fields based on pathlines.

2.2. *HCCI Combustion Simulation*

Figure 7(a) shows the volume renderings of the $\mathscr{A}$ and $|\nabla\mathscr{A}|$ fields computed based on streamlines and pathlines, respectively, for a combustion simulation. This dataset is taken from the simulation of homogeneous charge compression ignition (HCCI) engine combustion [6]. The domain has periodic boundary and is represented as a 640×640 regular grid. The 2D time-varying vector field consists of 299 time-steps with a time interval of 10^{-5} seconds. For the streamline based result (Figure 7(b)), we compute the 2D $\mathscr{A}$ fields at the individual time steps, respectively, and then stack these 2D fields to constitute a 3D volumetric $\mathscr{A}$ field. From this result, the translation of the vortices and their interaction (e.g., merging and splitting) can be easily discerned (see the accompanying video). For the pathline based result shown in Figure 7(b), we compute the 3D $\mathscr{A}$ field using the framework described in the paper. The $\mathscr{A}$ field highlights the regions in the flow where the trajectories (i.e., pathlines) of the particles exhibit strong rotation, while the $|\nabla\mathscr{A}|$ field indicates the boundaries of these different regions. In both streamline-based and pathline-based $\mathscr{A}$ field computations, the change of the flow direction is used for the accumulation.

References

[1] Shi, K, Theisel, H, Hauser, H, Weinkauf, T, Matkovic, K, Hege, HC, et al. Path line attributes - an information visualization approach to analyzing the dynamic behavior of 3D time-dependent flow fields. In: Hege, HC, Polthier, K, Scheuermann, G, editors. Topology-Based Methods in Visualization II. Mathematics and Visualization; Grimma, Germany: Springer. ISBN 978-3-540-88605-1; 2009, p. 75–88. doi:10.1007/978-3-540-88606-8_6.

[2] Haller, G. Lagrangian coherent structures and the rate of strain in two-dimensional turbulence. Phys Fluids A 2001;13:3365–3385.

[3] Okada, A, Kao, DL. Enhanced line integral convolution with flow feature detection. In: Electronic Imaging'97. International Society for Optics and Photonics; 1997, p. 206–217.

[4] Weinkauf, T, Theisel, H. Streak lines as tangent curves of a derived vector field. IEEE Transactions on Visualization and Computer Graphics (Proceedings Visualization 2010) 2010;16(6):1225–1234.

[5] Kasten, J, Reininghaus, J, Hotz, I, Hege, HC. Two-dimensional time-dependent vortex regions based on the acceleration magnitude. Transactions on Visualization and Computer Graphics (Vis'11) 2011;17(12):2080–2087.

[6] Hawkes, E, Sankaran, R, Pébay, P, Chen, J. Direct numerical simulation of ignition front propagation in a constant volume with temperature inhomogeneities: II. Parametric study. Combustion and Flame 2006;145:145–159.

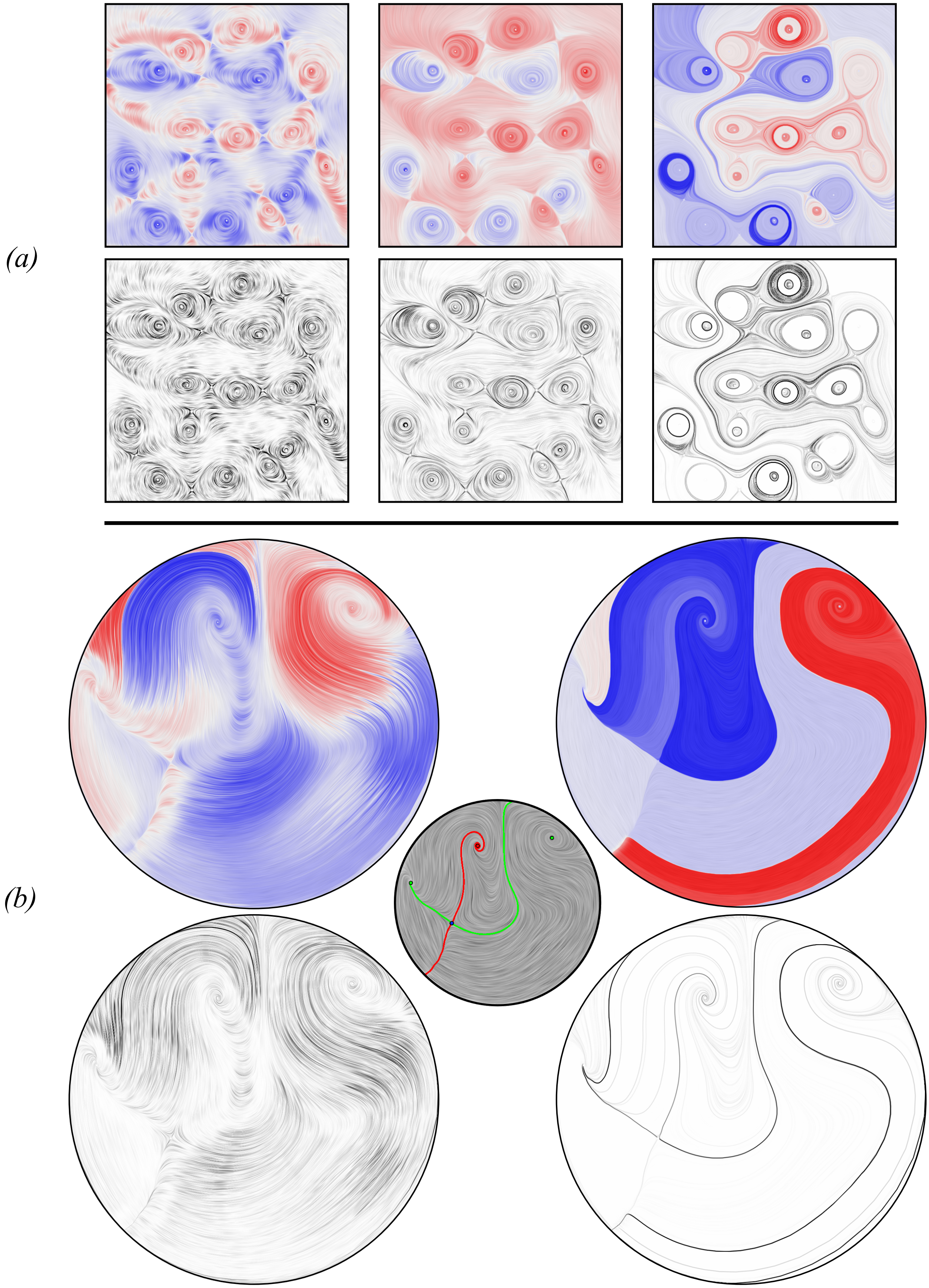

Fig. 1: (a) $\mathscr{A}$ (top) and $|\nabla\mathscr{A}|$ (bottom) fields of a synthetic flow with different window sizes for accumulation: (left) 10%, (middle) 40%, (right) 2,000% of the size of the bounding box of the data domain are used, respectively. (b) $\mathscr{A}$ (top) and $|\nabla\mathscr{A}|$ (bottom) fields of a 2D cross section of a diesel engine simulation with different window sizes for accumulation: (left) 10%, (right) 2,000% of the size of the bounding box of the data domain are used, respectively. The inset shows the topology of this 2D flow. Both $\mathscr{A}$ fields are obtained by accumulating the angle change of the flow direction.

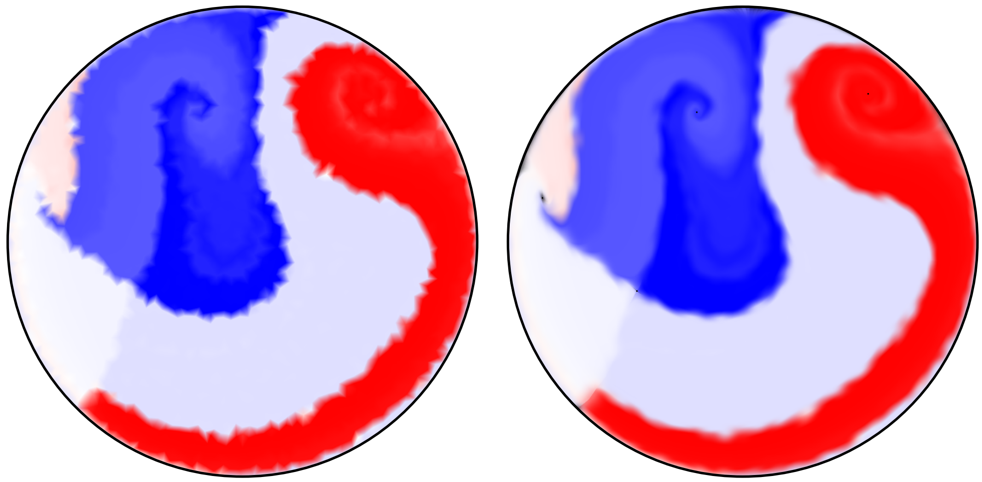

Fig. 2: (Left) shows an $\mathscr{A}$ field computed on a triangle mesh before smoothing. (right) shows the smoothing result.

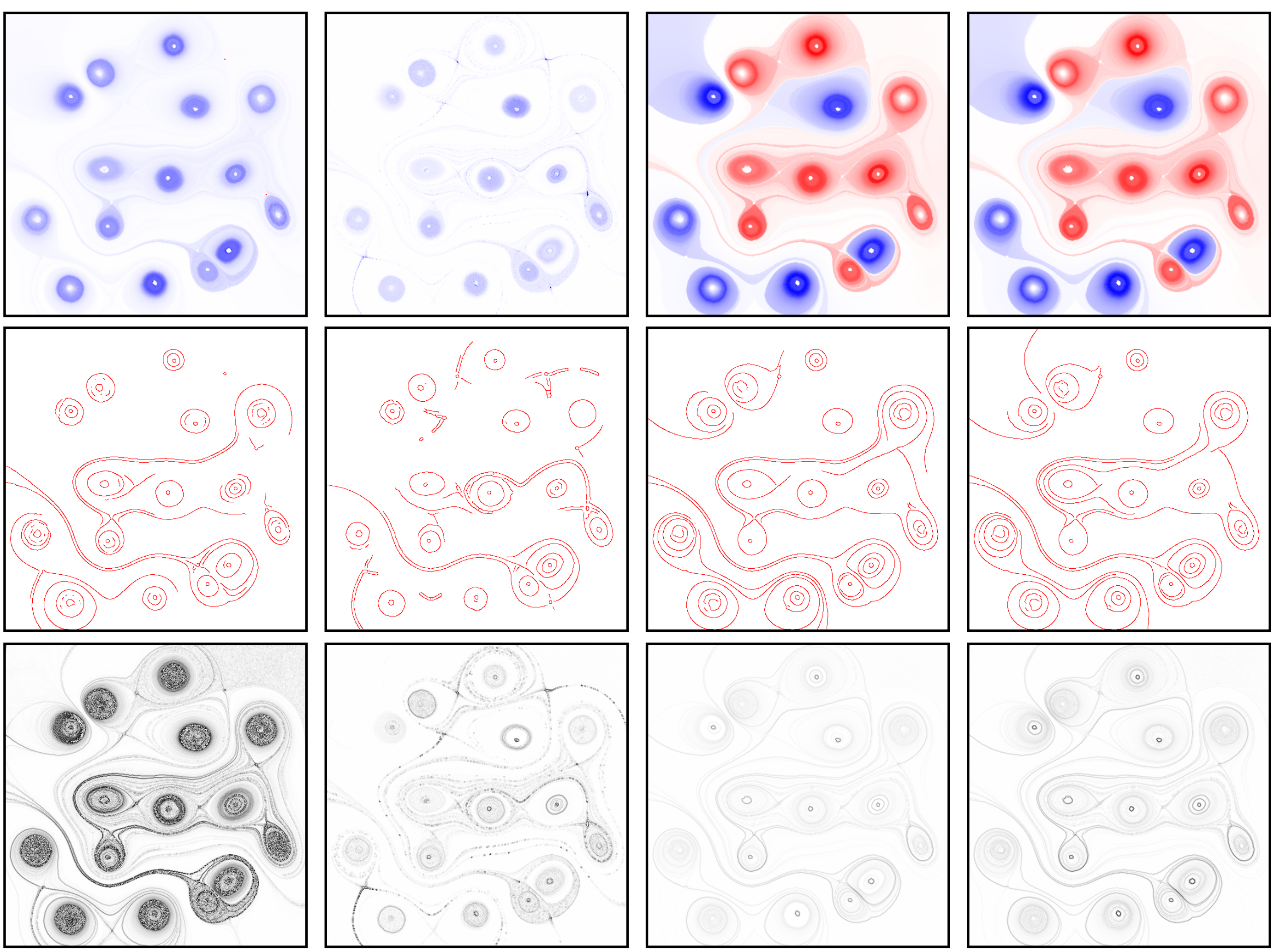

(a) lambda_2 (b) Q (c) curl (d) winding angle

Fig. 3: The comparison of the $\mathscr{A}$ fields of a synthetic flow data based on (a) λ_2, (b) Q, (c) curl, and (d) winding angle, respectively. The second row shows the detected edges using the Canny edge detector, and the third row shows the corresponding $|\nabla\mathscr{A}|$ fields.